Sources and distributions of dust aerosols simulated with the GOCART model

Paul Ginoux
Georgia Institute of Technology, Atlanta

Mian Chin
Georgia Institute of Technology, Atlanta

Ina Tegen
Max-Planck-Institute for Biogeochemistry, Jena, Germany

Joseph M. Prospero
Rosenstiel School of Marine and Atmospheric Science, University of Miami

Brent Holben
NASA Goddard Space Flight Center, Greenbelt

Oleg Dubovik
Science Systems and Applications, Inc., Lanham, Maryland

Shian-Jiann Lin
NASA Goddard Space Flight Center, Greenbelt

Short title: DUST AEROSOL MODELING

Abstract. The global distribution of dust aerosol is simulated with the Georgia Tech/Goddard Global Ozone Chemistry Aerosol Radiation and Transport (GOCART) model. In this model, all topographic lows with bare ground surface are assumed to have accumulated sediments which are potential dust sources. The uplifting of dust particles is expressed as a function of surface wind speed and wetness. The GOCART model is driven by the assimilated meteorological fields from the Goddard Earth Observing System Data Assimilation System (GEOS DAS) which facilitates direct comparison with observations. The model includes seven size classes of mineral dust ranging from 0.1 - 6 μm radius. The total annual emission is estimated to be between 1604 and 1960 Tg yr^{-1} in a 5-year simulation. The model has been evaluated by comparing simulation results with ground-based measurements and satellite data. The evaluation has been performed by comparing surface concentrations, vertical distributions, deposition rates, optical thickness and size distributions. The comparisons show that the model results generally agree with the observations without the necessity of invoking any contribution from anthropogenic disturbances to soils. But the model overpredicts the transport of dust from the Asian sources to the North Pacific. This discrepancy is attributed to an overestimate of small particle emission from the Asian sources.

1. Introduction

There is an increasing interest in the atmospheric transport of mineral dust. Recent research suggests that mineral dust may play an important role in climate forcing by altering the radiation balance in the atmosphere [*Tegen et al.,* 1997] and by affecting cloud nucleation and optical properties [*Levin et al.,* 1996]. In addition, dust can serve as a catalyst for reactive gas species in the atmosphere [*Dentener et al.*, 1996] and can significantly modify photochemical processes [*Dickerson et al.,* 1997]. Large amounts of mineral dust are deposited to the oceans [*Duce,* 1995; *Prospero,* 1996] where it potentially plays an important role in biogeochemical processes.

Many studies, which have characterized dust generation on a micro-meteorological scale, have shown that dust mobilization is sensitive to a wide range of factors including the composition of the soils, the soil moisture content, the surface conditions and wind velocity. Previous global models have identified the dust sources based on the soil moisture content [*Joussaume,* 1990], the location of deserts from vegetation data set [*Genthon,* 1992a, b; *Mahowald et al.,* 1999], the location of sparsely vegetated area and soil texture from vegetation and soil data sets [*Tegen and Fung,* 1994], or the distribution of dust storm frequencies over arid regions [*Dentener et al.,* 1996]. Discrepancies between simulated and observed dust loading have led some modelers to invoke land surface modification as a source that contributes as much as 50% of total dust emission [*Tegen and Fung,* 1995].

In this work, we determine the global distribution of dust sources by using the surface topographic features. We assume that the most probable sources are related to the degree of depression. The dust sources estimated here are consistent with the recent study of *Prospero et al.,* [2000]. In that study, using the long-term (1979-present) record of the global aerosol index retrieved from the Total Ozone Mapping Spectrometer (TOMS) instrument [*Herman et al.,* 1997, *Torres et al.,* 1998], *Prospero et al.* [2000] have identified the location of all the major dust sources. They have shown that the

sources can usually be associated with topographic lows which have a deep accumulation of alluvial sediments formed during the late Pleistocene or Holocene. These sediments are composed of fine particles which are easily eroded by winds.

To simulate the atmospheric dust distribution, emission, transport and deposition of seven particle size classes between 0.1 and 6 μm radius have been incorporated in the Georgia Tech/Goddard Global Ozone Chemistry Aerosol Radiation and Transport (GOCART) model. This model is driven by assimilated meteorological fields generated in the Goddard Earth Observing System Data Assimilation System (GEOS DAS) and has been applied to simulate atmospheric sulfate aerosols and its precursors [*Chin et al.,* 2000]. The advantage of the GOCART model is that, by using observed meteorological fields, it can effectively simulate atmospheric constituents for any specific time period.

In this paper, we present a detailed description of the components incorporated in GOCART model to simulate dust distributions. The global distribution and budget of mineral dust is discussed. Results from our model simulations are compared with ground-based and satellite measurements. The comparisons include the surface concentrations, vertical distribution, deposition fluxes, optical thickness and size distribution. We also compare our results with those of other model studies. This paper is focusing on the model evaluation on the global scale and its ability to reproduce the observed seasonal cycle. The detailed regional and daily analysis of the model results with TOMS aerosol index will be discussed in a separate paper.

2. Model description

2.1. Model configuration

The GOCART model has been developed by *Chin et al.* [2000] to simulate the distribution of sulfur species in the atmosphere. The model solves the continuity equation which includes the emission, chemistry, advection, convection, diffusion, dry

deposition and wet deposition of each species.

The meteorological fields used to drive the GOCART model are assimilated data by GEOS-DAS [*Schubert et al.,* 1993]. The GOCART model has the same horizontal resolution as GEOS DAS: 2^o latitude by 2.5^o longitude. The vertical resolution varies with the different GEOS DAS versions. For GEOS DAS version 1, available from February 1980 to November 1995, there are 20 vertical sigma levels from the Earth's surface to 10 mb. For GEOS DAS version 1.3, available from April 1995 to November 1997, the data fields have been regridded from the original 46 levels into 26 vertical levels from the Earth's surface to 0.1 mb, with 23 levels in the troposphere. The GEOS DAS prognostic variables are instantaneous values saved every 6 hours, while the diagnostic fields are averaged values over 3 or 6 hours, as indicated in Table 1. Values of instantaneous fields are linearly interpolated to every model time step (20 minutes). The model is initialized with near zero mass and is spin-up for one month prior to the simulations, and the results are saved every 6 hours.

2.2. Particle sizes

Mineral particles in the atmosphere have radii ranging from about 0.1 to 50 μm [*Duce,* 1995]. The uplifting of particles smaller than 0.1 μm by air is limited by the adhesive and cohesive forces which tend to form larger particles or aggregates [*Scheffer and Schatschabel,* 1992]. Because of gravitational settling, particles larger than 6μm generally have short atmospheric lifetimes (i.e., less than a few hours) [*Tegen and Fung,* 1994] and limits their significance on the global scale. The present study is therefore restricted to particles with a diameter larger than 0.1μm and smaller than 6 μm radius. Following *Tegen and Lacis* [1996] the size distribution is modeled into seven size bins, and the mass distribution varies linearly with respect to radius in each bins. The seven size ranges are 0.1-0.18 μm, 0.18-0.3 μm, 0.3-0.6 μm, 0.6-1 μm, 1-1.8 μm, 1.8-3 μm, and 3-6 μm, with corresponding effective radii of 0.15, 0.25, 0.4, 0.8, 1.5, 2.5 and 4 μm,

respectively.

The U.S. Department of Agriculture (USDA) defines particles with a radius between 1 μm and 25 μm as silt, and below 1 μm as clay [*Hillel,* 1982]. Mineralogical silt particles are mainly composed of quartz but they are often coated with strongly adherent clay such that their physicochemical properties are similar to clay [*Hillel,* 1982]. The mass density of clay (classes 1-4) and silt (classes 5-7) are 2.5 and 2.65 g m^{-3}, respectively.

The size distribution of small particles (radius 0.1-1 μm) is assumed not to change during transport, since the differences in the gravitational settling velocities within this size class are small. For numerical efficiency the first four classes are transported as one group (0.1-1 μm) of clay particles with an effective radius of 0.75 μm. When computing optical properties, which have a strong dependency on the size distribution, the clay size class is redistributed into the original four classes (0.1-0.18, 0.18-0.3, 0.3-0.6 and 0.6-1 μm) by assuming a mass fraction for each class: 0.9, 8.1, 23.4, and 67.6%, respectively [*Tegen and Lacis,* [1996].

2.3. Dust sources

The origin of clay minerals at the Earth's surface is, in the majority of cases, a process of weathering of rocks to form alluvium (stream deposited sediments) [*Velde*, 1992]. Because there is no data on the global distribution of alluvium over the land surfaces, the potential location of accumulated sediments has been determined by comparing the elevation of any $1^o \times 1^o$ grid point with its surrounding hydrological basin. The complex contours of each basin have been simplified by assuming a constant area of $10^o \times 10^o$. This choice is based on the fact that most hydrological basin has a size of roughly 10 degrees in the arid regions. A more precise source distribution should be based on a more accurate basin contouring by using a hydrological model.

We assume that a basin with pronounced topographic variations contains large amount of sediments which are accumulated essentially in the valleys and depressions,

and over a relatively flat basin the amount of alluvium is homogeneously distributed. We introduce here a source function S, which is the fraction of alluvium available for wind erosion, as follows:

$$S = \left(\frac{z_{max} - z_i}{z_{max} - z_{min}} \right)^5 \quad (1)$$

Where S is the probability to have accumulated sediments in the grid cell i of altitude z_i, and z_{max} and z_{min} are the maximum and minimum elevations in the surrounding $10^o \times 10^o$ topography, respectively. It is not intended here to calculate the exact amount of alluvium but rather to define the most probable locations of sediment. To increase the topographic contrast of these locations and to obtain the best fit with the sources identified by *Prospero et al.,* [2000], the relative altitude has been taken at the fifth power. Only land surface with bare soil is considered as possible dust sources. We identify the bare soil surface from the $1^o \times 1^o$ vegetation data set derived from the Advanced Very High Resolution Radiometer (AVHRR) data [*DeFries and Townshend,* 1994].

Figure 1 shows the global distributions of the source function S, regridded on the $2.5^o \times 2^o$ GOCART grid, the calculated dust emission (see next section), and the TOMS aerosol index. Most of the maxima of the S function are collocated with the "hot spots" of the TOMS aerosol index which have been identified as dust sources by *Prospero et al.* [2000]. The clearest examples are the Tunisian, Libyan, Mauritanian and Malian sources in the Sahara, the Bodele depression in the Sahel, the Indian source along the Indus valley, the Taklimakan located North of the Himalaya, the Lake Eyre basin in Australia, the Salton Sea in southern California, the Altiplano and Patagonia in the Andes, and the Namibian source in South-West Africa.

2.4. Dust emission

Dust uplifting into the atmosphere is mainly initiated by saltation bombardment (sand blasting). *Marticonera and Bergametti* [1995] have developed a model of dust

emission based on a complex parameterization of this process. Their emission scheme has been incorporated in dust transport model for regional studies [*Schulz et al.,* 1998; *Guelle et al.,* 2000]. The major limitation of this algorithm is that it needs detailed informations of soil characteristics which are not readily available on the global scale.

We use an equivalent empirical formulation by *Gillette and Passi* [1988] for dust uplifting which requires the knowledge of the surface wind speed and the threshold velocity of wind erosion. In this formulation the flux F_p of particle size class p is approximated by the expression:

$$F_p = \begin{cases} C \times S \times s_p \times u_{10m}^2 \times (u_{10m} - u_t) & \text{if } u_{10m} > u_t \\ 0 & \text{otherwise} \end{cases} \tag{2}$$

where C is a dimensional factor equal to 1 μg s^2 m^{-5}, S is the source function described in section 2.3, u_{10m} is the horizontal wind speed at 10 meters, u_t is the threshold velocity, and s_p is the fraction of each size class which is defined below.

The fractions of clay and silt sizes are different for different soil types at each location. Due to the uncertainties in the available soil texture data, we choose a simple particle size distribution, following *Tegen and Fung* [1994]. The fraction of clay is based on the assumption that erodible clay represents 1/10 of the total mass of emitted silt, and that of each silt sub-class is assumed to be the same. The s_p values are thus 0.1 for the class 0.1-1μm, and 1/3 for the classes 1-1.8μm, 1.8-3μm, and 3-6μm, respectively.

The main factor affecting the threshold velocity u_t is the interparticle cohesion forces which depends on the particle size and the soil moisture [*Pye,* 1989]. *Belly* [1964] suggested a relationship for entrainment of sand which takes into account the particle size and soil moisture content. This relationship has been modified here to use the surface wetness (provided by GEOS DAS) in determining the threshold wind velocity:

$$u_t = \begin{cases} A\sqrt{\frac{\rho_p - \rho_a}{\rho_a} g \Phi_p}(1.2 + 0.2 \log_{10} w) & \text{if } w < 0.5 \\ \infty & \text{otherwise} \end{cases} \tag{3}$$

where $A = 6.5$ is a dimensionless parameter, w is the surface wetness [0.001-1], Φ_p is the particle diameter, g is the acceleration of gravity, ρ_p and ρ_a are the particle and air density, respectively. The typical values of w in arid regions are between 0.001 and 0.1, but are higher than 0.5 after precipitation. For w=0.1, u_t is 1.5 m s^{-1} for the smallest class and 3 m s^{-1} for the largest class. This formulation, based on studies for large sand particles ($r > 30\mu$m) shows an increase of u_t with increase of particle size. But wind tunnel and field experiments [*Iversen and White,* 1982; *Marticonera and Bergametti,* 1995; *Shao et al.,* 1996] have shown that for particle $r < 35\mu$m, u_t decreases with the increase of radius. Therefore, the threshold velocity obtained from equation (3) will be lower than that from wind tunnel experiments, and the corresponding dust emission will be larger.

In Figure 1, the similarity between the source distribution (upper panel) and the annual dust emission averaged from 1987 to 1990 (middle panel) shows the importance of the source function (S) relative to the other variables in equation 2.

2.5. Removal processes

Two types of removal processes are considered, the dry deposition which includes the turbulent transfer to the surface and gravitational settling, and the wet deposition which includes rainout and washout in and below clouds .

The turbulent transfer of particles at the surface is calculated as a first order process using a deposition velocity v_d. The velocity v_d is assumed to be equivalent to the exchange velocity for heat and moisture at the surface. This exchange velocity is diagnosed from flux profile relationships and is available in the GEOS DAS data [*Takacs et al.,* 1994]. However, particles which are deposited at the surface can be uplifted outside source regions depending on the surface wetness w and the wind velocity. To

take into account this fact, we define an effective dry deposition velocity $\hat{v}_d$ as follows

$$\hat{v}_d = \begin{cases} v_d \left(w + (1-w) \times \exp[-(u_{10m} - u_t)]\right) & \text{if } u_{10m} > u_t \\ v_d & \text{otherwise} \end{cases} \quad (4)$$

In this formula, $\hat{v}_d$ will be smaller than v_d with strong surface wind speed over dry surface. Over wet surfaces, $\hat{v}_d$ is equal to v_d.

For large aerosols the most efficient removal process is gravitational settling. The change of concentration by gravitational settling is calculated by an implicit scheme at all vertical levels. The settling velocity v_{stk} for a particle of radius r is determined using the Stokes law:

$$v_{stk} = \frac{2}{9}\frac{\rho_p g}{\mu} r^2 C_{Cunn} \quad (5)$$

where ρ_p is the particle density, g is the acceleration of gravity, and μ is the absolute viscosity of the air (1.5 10^5 kg $m^{-1}.s^{-1}$), and C_{Cunn} is the Cunningham correction which takes into account the viscosity dependency on air pressure and temperature [*Fuchs,* 1964].

Wet scavenging in the model includes rainout (in-cloud precipitation) and washout (below cloud precipitation) in large-scale precipitation and in deep convective cloud updraft. The parameterization of these processes for sulfate aerosols has been described in detail by *Chin et al.* [2000]. Unfortunately, there are few data concerning the scavenging efficiency of dust particles. Here we use the same wet scavenging parameters for dust as those used for sulfate, which is probably reasonable, since the scavenging efficiency reported by *Galloway et al.* [1993] for non-sea-salt sulfate and nitrate are roughly the same as the values used by *Duce* [1991] for dust over the North Atlantic ocean.

2.6. Transport

Dust particles are transported in the atmosphere by advection, convection and turbulent mixing. The different methods use to solve these processes have been described

elsewhere [*Allen et al.,* 1996; *Chin et al.* 2000]. Here, briefly, advection is computed by a flux-form semi-Lagrangian method [*Lin and Rood,* 1996]. Moist convection is parameterized using archived cloud mass flux fields from the GEOS DAS. Turbulent mixing due to mechanical shear and buoyancy is approximated by eddy diffusion. The eddy diffusion coefficient is calculated using a 2.5 order local closure parameterization [*Helfland and Labraga,* 1988].

3. Model results

The dust distribution has been simulated over several time periods: 1987-1990, 1996, most of 1997 and a few months in 1994. The choice of these periods is based on the available data sets used for comparison. In this section, we present the global budget of dust and compare the model results with observations. The observed data sets have been selected for their adequate temporal and spatial coverage. These data sets can be separated into surface measurements (concentration and deposition flux), vertically integrated ground-based observations (size distribution and optical thickness), and satellite data (vertical distribution and optical thickness).

3.1. Global budget

Table 2 gives the annual budget for 5 years, 1987-1990 and 1996. The averaged global dust emission is 1814 Tg yr^{-1}. The calculated emission ranges from 1604 Tg yr^{-1}) in 1996 to 1956 Tg yr^{-1} in 1988, reflecting mainly the differences in the wind speed at 10 meters. The calculated emissions are within the range of previous model estimates with similar sizes range: 1250 Tg yr^{-1} for particles radius less than 8 μm [*Tegen and Fung,* 1995], 1800 Tg yr^{-1} for particles less than 10 μm [*Dentener et al.,* 1996], and 3000 Tg yr^{-1} for a single class centered at 1.25 μm [*Mahowald et al.,* 1999]. Dry deposition is the main loss process with an averaged value of 1607 Tg yr^{-1}. Wet deposition accounts for 235 Tg yr^{-1} and represents only 10% of the total loss. The atmospheric dust load is

36 Tg with an averaged lifetime of about 1 week. Table 3 lists the budget and lifetimes for each size class. The highest emission is obtained for particles radii ranging from 1 to 2 μm. The lifetime of the two smallest classes is 2 weeks and drops to 1 day for the largest class (3-6 μm). Our estimated lifetime for the smallest particles is 50% longer and for the largest particles is 50% shorter than the values reported by *Tegen and Lacis,* [1996]. The differences can be explained by a stronger dry deposition rate and a weaker wet deposition rate in our case. While the lifetime of particles size 1-2 μm agrees with *Tegen and Lacis* [1996], it is twice the value reported by *Mahowald et al.* [1999]. However, *Mahowald et al.* [1999] considered only one dust size class that may result in a shorter lifetime.

The simulated total annual deposition to various ocean regions are compared in Table 4 with *Duce at al.* [1991] and *Prospero* [1996] estimations from in-situ measurements. *Duce at al.* [1991] use a scavenging ratio for dust of 200 for the North Atlantic ocean and 1000 over the remainder of the world ocean. *Prospero* [1996] has suggested to use a scavenging ratio of 200 for all ocean regions. Our calculated total annual deposition over the North Pacific and North Atlantic are comparable to that estimated by *Prospero* [1996]. But over the other oceans, the model results are closer to values estimated by *Duce at al.* [1991]. The major difference is over the North Indian ocean where the simulated total deposition is 8 times higher than the value estimated by *Prospero* [1996]. As mentioned by the author, there is a large uncertainty in the estimated value because there were very few data over the Indian ocean.

3.2. Dust concentrations in the boundary layer

The calculated seasonal dust concentrations in the planetary boundary layer (0 to 1 km altitude) are shown in Figure 2. These values have been averaged over 5 years (1987-1990 and 1996). The source regions appear clearly in this figure as well as the patterns due to long range transport. The highest concentrations (above 250 μg m^{-3})

are located in the northern Hemisphere: over the western Sahara and the Sahel region, in part of the Arabic Peninsula and Iran, and in the Asian source regions (Taklimakan and Gobi deserts). Over North America, there is a less pronounced maximum which is centered on the Salton sea in southern California. In the southern Hemisphere, the peak values are located in the regions of the Lake Eyre basin (Australia), Altiplano (Bolivia), Patagonia (Argentina) and Namibia (South Africa). These maxima are quite persistent through the seasons. The model shows a clear latitudinal shift of the dust plume over the North Atlantic from winter to summer. This seasonal shift is related to the movements of the Intertropical Convergence Zone (ITCZ) which occupies its southernmost position in winter ($\sim 5^o$N) and northernmost position in summer ($\sim 20^o$N). The seasonal shift in the model matches that observed by satellite instruments, such as the Advanced Very High Resolution Radiometer (AVHRR) [*Husar et al.* 1997].

The surface concentrations are similar to the values calculated by *Dentener et al.* [1996] over North Africa with maxima over the Sahel and Sahara, but they differ significantly elsewhere. The most striking difference is over the Taklimakan desert which is a regional minimum in *Dentener et al.* [1996] but a maximum in Figure 2. Another important difference is near the sources in the southern hemisphere where the GOCART model surface concentrations are significantly higher than *Dentener et al.* [1996], except over Australia. The comparison with *Tegen and Fung* [1994] indicates some differences in Africa where the Sahel source was not included in their study and in Australia where the surface concentrations from their model were as high as over the Sahara.

The monthly dust concentration has been compared with the observations at 18 sites indicated in Figure 2 with their number. These sites were operated by the University of Miami [*Prospero,* 1996]. Some sites are located close to the source regions: Izana (station 4) near North Africa, Kaashidhoo (8) near India, Cheju (9) and Hedo (10) in the Asian east coast, Cape Grim (17) near Australia, and Cape Point (7) in South Africa. Other sites are located downwind of the source regions: Barbados (1),

Miami(2), and Bermuda (3) along the Saharan dust plumes; Enewetak (11), Midway (12) and Oahu (13) in the corridor of Asian and North American plumes; Norfolk Island (18) and New Caledonia (16) downwind of the Australian dust sources. The remaining sites are located in remote regions of the North Atlantic, Mace Head (5); South Atlantic, King George (6); and Pacific, Nauru (14) and Funafuti (15). Most data have been collected in the 1980's and 1990's, but the period of measurements varies betwen sites. The locations of the 18 sites are given in Table 5.

Figure 3 shows the comparison of the annually averaged dust concentrations measured and simulated at the 18 sites where the model results are 5 years (1987-1990, 1996) averaged values. The annual concentrations vary by more than 3 orders of magnitude from more than 30 μg m^{-3} at Izana to less than 0.1 μg m^{-1} at Nauru Island. The sites can be divided into two groups depending on the range of surface concentrations: the dusty sites with values greater than 2 μg m^{-3} and the remote sites with values less than 2 μg m^{-3}. The model concentrations agree with the observations to within a factor of 2 in the dusty regions but the model overestimates the concentration in the remote regions, particularly in the North Pacific. For example, dust concentration at Midway (12) is overestimated by as much as a factor of 5. Part of this discrepancy is due to the fact that this site was operated with sector control so that the samples were taken only when the winds came from the ocean. However, such sampling bias may not explain a factor 5 difference between the model and the data.

The good agreement in the dusty regions and the large discrepancy in the remote Pacific suggest a somewhat deficient representation of the transport, removal processes or the size distribution in the model.

Figure 4 shows the seasonal variation of dust concentration at each of the 18 sites, with 11 sites (1, 2, 3, 4, 5, 8, 9, 10, 11, 12 and 13) in the northern hemisphere and 7 sites (6, 7, 14, 15, 16, 17 and 18) in the southern hemisphere.

3.2.1. Northern hemisphere.

Over the dusty regions, the model reproduces the seasonal variation although sometimes the observed values are underestimated. For example, the June maximum at Barbados is underestimated by 50%. Further away from the African dust source, at Miami and Bermuda, the model results are within the standard deviation of the observed values. The differences between these 3 sites can be due to sub-gridscale local meteorology or to the fact that the measurements have been averaged over different periods. Another example is at Cheju: the Spring maximum is well reproduced but is underestimated by 50%. Similarly, the model fails to capture the dust peak in April at Hedo.

A difficulty in assessing the model results at the surface is that it is not necessarily representative of dust concentration aloft where most dust plumes are traveling. Transport aloft is tested with data from Izana (Site 4 in Figure 2) which is located about 2.5 km above sea level. Measurements at this location are considered to be representative of most African dust plumes [*Chiapello et al.,* 1997]. The observed concentrations at Izana are the largest of the 18 sites. The simulated concentrations are within the observed standard deviations except in December and January. But the simulated standard deviation is particularly large during these two months. This comparison shows no indication of overprediction of dust concentration aloft from the African sources. The situation in Asia is generally different from that in Africa. The Taklimakan desert, which is the major Asian dust source [*Zhang et al.,* 1998], is located between 1 and 2 km above sea level. There is evidence that Asian dust is transported around 8 km altitude [*Merrill et al.,* 1989]. The long range transport at such a high altitude is much more rapid than commonly found for African dust plumes ($\sim$ 3-5 km altitude) [*Karyampudi et al.,* 1999]. An overprediction of dust emission from the Taklimakan will have a longer and stronger impact on the remote atmosphere than from African dust sources. To better understand the origin of the discrepancy over the North Pacific, it is necessary to validate the emission rates and dust loads close to the Asian

sources and the altitude of the traveling plumes. This will be discussed in the next sections.

3.2.2. Southern hemisphere.

In the southern hemisphere, the model simulates the seasonal cycle at the different sites downwind of the dust sources reasonably well (sites 6, 7, 14, 15, 16, 17 and 18 in Figure 4). At Cape Grim, South-East of the Australian dust source, the model reproduces the seasonal cycle of dust concentration, although the austral summer maximum is underpredicted by a factor of 2. Further East, at Norfolk Island, the austral winter minimum is overpredicted by a factor of 2. At Cape Point, near the Namibian dust source, the model simulates correctly, within the standard deviation, the increase of concentration from March to July. Finally, at King George which is influenced by dust emission from Patagonia, the model is able to reproduce the weak seasonal cycle with a slight increase in January and December. The two observed high peaks in January and April are due to dust events generated during the limited period of measurements.

To summarize these comparisons, we conclude that the model reproduces the dust concentration and seasonal variations at most sites, but overpredicts the dust levels from Asian dust sources over the tropical and subtropical Pacific by a factor of 2 to 5. This overestimation probably applies to the higher latitudes of North Pacific as well. This discrepancy could be related to a misrepresentation of the altitude of the Asian dust plumes, dust emissions from the Asian sources, or the removal rates.

3.3. Vertical distribution

Figure 5 shows the 4-year (1987-1990) zonally averaged dust concentrations in the model. Dust concentration generally decreases rapidly with height. In the free troposphere zonal mean concentrations range from near 0 to 5 μg m^{-3}. Figure 5 presents some differences with the model results reported by *Dentener et al.* [1996]. We obtain a stronger northward meridional transport to high latitudes at around

800 mb, particularly in the North hemisphere. *Tegen and Fung* [1994] obtained also a meridional transport but at higher altitude (around 100 mb). Although there is considerable evidence of long range transport to high northern latitudes, for example in Norway [*Franzén et al.,* 1994] and Greenland [*Davidson et al.,* 1993], there are few direct measurements of dust vertical distribution.

The most useful data with which to compare the model vertical distribution are the aerosol backscattering measurements made during the Lidar in Space Technology Experiment (LITE) [*Winker et al.,* 1996]. The data covers 10 days in September 1994. The lidar return signal was sampled at 10MHz, corresponding to a spatial resolution of 15 meters between the Earth's surface to 20 km altitude. The data used for comparison are the backscattering ratio at 532 nm (http://www-lite.larc.nasa.gov). The orbits passing over western Sahara (orbit 115) and the Taklimakan desert (orbit 125) have been selected for comparison with model simulations. Plate 1 shows the backscattering ratio measured along the orbits 115 (17 September 1994, 1 am) and 125 (17 September, 4 pm) and the corresponding simulated dust concentrations from the sea-level to 10 km altitude. The LITE orbit 115 signal shows the African plume which rises over the African west coast and extends to 5 km altitude (first panel). The strong signal near the ocean surface is due primarily to other types of aerosols (e.g. sea-salt). As seen in the second panel of Plate 1, the model reproduces the vertical and horizontal extension of the dust plume, and the location of the dust source in the model is located correctly at between 18.5 and 20°N. The last two panels in Plate 1 are the vertical distributions along the orbit 125 over China. The LITE data (third panel) show a dust plume extending to 7-8 km altitude as well as dust mixed in the boundary layer. The model can reproduce this extension, but does not capture the pronounced feature at 3-4 km (last panel). These results indicate that dust particles emitted from the Asian sources are uplifted more efficiently than over the Sahara to high altitude in the jets where they are subjected to efficient long range transport. Such results have been previously

suggested (e.g. *Merrill et al.,* [1989]).

3.4. Dust deposition

Figure 6 shows the annual total deposition (dry and wet deposition) averaged over 5 years (1987-1990 and 1996). In this figure, a latitudinal gradient appears clearly, with a maximum between 0^o and 45^oN, and a minimum below 45^oS. The highest deposition is over western China with a maximum of 162 g m^{-2} yr^{-1}.

Figure 7 shows the comparison between the annual observed and simulated removal rate at 16 sites. The site location, period of measurements, and the observed and simulated values of the total annual deposition flux are given in Table 6. The 16 sites are also indicated in Figure 6 with their number. The range of observed values varies from 450 g m^{-2} yr^{-1} over the Taklimakan to 0.08 g m^2 yr^{-1} in equatorial Pacific.

Figure 7 shows that the model successfully predicts high versus low deposition ranging over 4 orders of magnitude, although it tends to underpredict the highest values and overpredict the lowest values. The underpredicted values over the Taklimakan (15), Tel-Aviv (16) and Spain (3) are most likely due to the contribution of particles larger than 6 μm (largest simulated particle radius). The closer the measurements to the source the higher the fraction of large particles. Observed deposition fluxes at three closely located sites 12, 13 and 14 vary by a factor of 5 while the model shows only 20% differences. This indicates that there is a large local variability in deposition rates that is not resolved by the model. Despite this fact, we conclude that the deposition fluxes are in general simulated reasonably well.

3.5. Optical thickness

The optical thickness τ is calculated from the dust mass load by the relation

$$\tau(\lambda) = \sum_i \frac{3}{4} \frac{Q_{ext}(\lambda, r_i) M_i}{r_i \rho_i} \tag{6}$$

where $Q_{ext}(\lambda, r_i)$ is the extinction efficiency factor at wavelength λ and effective radius r_i, M_i is the column mass loading for the size class i, and ρ_i is the mass density of the size class i. The values of $Q_{ext}(\lambda,\ r_i)$ are calculated using Mie theory and assuming lognormal size distributions [*Chin et al.,* 2001].

3.5.1 Comparison with AVHRR data.

The global distribution of the aerosol optical thickness has been retrieved at 630 nm from the AVHRR instrument [*Husar et al.,* 1997]. Due to the large variability of land surface reflectance in the visible range, only information over the ocean can be retrieved. The optical thickness has been derived assuming a single scattering albedo equal to 1 which leads to underestimate the true value. Although the AVHRR measures total aerosol optical thickness, dust is the major aerosol component at several regions such as the tropical-subtropical North Atlantic, western Pacific and Arabian sea.

Figure 8 shows the mean optical thickness at 650 nm in comparison with the mean AVHRR optical thickness at 630 nm from 1987 to 1990. The comparison shows that the calculated optical thickness corresponds well to the observed values over the dust dominated oceanic regions. The model reproduces correctly three major dust plumes extending over the North Atlantic, the Arabian Sea, and the North Pacific. The simulated background values of optical thickness in the North hemisphere are between 0.05 and 0.1 which is comparable to the observed values. Due to the significant contribution of other aerosol types which have not been included in this work, it is possible that the model overestimates the background value in the remote regions of the northern hemisphere. The observed high values in the tropical regions is due to biomass burning aerosols which are not simulated.

It has been reported from the AVHRR data that the location of the aerosol plume in the tropical North Atlantic shifts with the seasons [e.g., *Rao et al.,* 1988]. In their modeling study *Tegen and Fung* [1995] suggested that emissions from human disturbed soils had to be included in the model in order to reproduce the observed seasonal

shift. On the other hand, recent studies have shown that it is the combination of biomass burning and dust aerosols that causes the seasonal shift [*Takamura et al.,* 2000; *Chin et al.,* 2001]. To understand the dust contributions, Figure 9 shows the monthly variation of the latitudinal position of the maximum dust aerosol optical thickness along the 25^{o}W meridian. From this figure, it appears that the model reproduces the observed latitudinal shift in 1989 and 1990. But in 1987 and 1988 from late fall to early spring, the simulated latitude of the dust plume is located further North. The difference is particularly significative in March 1988. To understand this difference we have analyzed the daily distributions. From this analysis, it appears that the GOCART model simulates an intense dust plume originating from the West Sahara and moving to Europe over the last week of March 1988, in agreement with the TOMS aerosol index. For the same period, the TOMS aerosol index has maxima over Nigeria and Ghana, South of 10^{o}N. These maxima indicate the presence of biomass burning activities.

From this comparison, it seems that the contribution of dust load to the aerosol optical thickness is generally not suffisant to explain the interannual variability of the latitudinal shift of the aerosol plume over the North Atlantic. The emission of other aerosol types by biomass burning is the major factor to explain maximum optical thickness South of 10^{o}N over the Atlantic in winter. But, due to the interannual variability of fire activities and surface wind conditions, the maxima of dust load and aerosol optical thickness can occasionally correspond in winter, as it was for the years 1989 and 1990. The low latitude of dust plumes is simulated without the necessity of invoking any contribution from anthropogenic disturbances to soils.

3.5.2. Comparison with AERONET data.

The simulated optical thickness has been compared with the Aerosol Robotic Network (AERONET) data. AERONET is a federated worldwide network of sun-photometers that are monitored and maintained at the NASA-Goddard Space Flight Center [*Holben et al.,* 1998]. Data have been collected since 1993, but most sites have

been operational after 1996. All the AERONET values used in this comparison have been screened for cloud-free conditions [*Smirnov et al.,* 2000a]. This screening have rejected a substantial number of data. To avoid bias, the comparison is based on model results extracted for the days when cloud-screened data are available. We select 6 sites where dust is considered to be the dominant aerosol type, although the contribution of other aerosol types can be significant. The presence of other aerosols can be detected on the basis of the wavelength dependency of optical depth. The Angstrom parameter α can be used as a first-order indicator of spectral extinction behavior [*Eck et al.,* 1999]. The empirical expression of α is given as

$$\alpha = -\frac{\ln\left(\frac{\tau_2}{\tau_1}\right)}{\ln\left(\frac{\lambda_2}{\lambda_1}\right)} \tag{7}$$

where τ_2 and τ_1 are the optical thickness at wavelength $\lambda_1(440nm)$ and $\lambda_2(670nm)$, respectively. In general, the smaller the particle size, the stronger the wavelength dependence, thus the larger the α values. Typical values of α range from >2 for smoke particles and pollution aerosols to nearly zero for high optical thickness dust particles [*Holben et al.,* 1991].

Figure 10 shows the comparison of optical thicknesses calculated at 450 nm from the model results and observed at 440 nm at six AERONET sites. The α values retrieved at these sites are also shown in Figure 10 for indication of particle sizes. Table 7 shows the location, selected period of measurements for each site, and the corresponding simulation period.

At Barbados, the model simulates the observed seasonal variation of optical thickness within the standard deviation. The observed June 1997 maximum is shifted to July by the model, but the simulated values are well within the observed standard deviation. *Smirnov et al.* [2000b] have studied in detail the AERONET data over Barbados and found a high correlation between the monthly mean optical thickness and dust concentration at the surface. Figure 4 shows that the model captures the observed

maximum surface concentration in June (1987-1990 and 1996). The discrepancy between the model and observations in June 1997 is thus not systematic but is most likely related to the variation of calculated emission rates in 1997.

The Cape Verde site is close to the Saharan dust source. At this site, the model reproduces, within the standard deviation, the observed optical thickness, at the exception of June 1997. For this month, the α parameter is around 0.1 which is characteristic for dust and the discrepancy cannot be attributed to the presence of other aerosols. It is most likely due to strong perturbations over the dust source which were not resolved in the model.

The Banizoumbou site is South-West of the Bodele depression and is representative of the Sahelian dust sources. The model reproduces the seasonal cycle within the standard deviation except in April where it underestimates the optical thickness by a factor of 3. The explanation given for the discrepancy at Cape Verde, June 1997, can also be given for this case.

At Sde Boker (Israel) and Barhain, the model reproduces the seasonal variation within the standard deviation. However, the α values at both sites are generally high, indicating the presence of sub-micron particles. The dust optical thickness is probably overestimated in the model.

At Dalanzadgad (Mongolia), the simulated optical thickness is higher than observed by as much as a factor of 2 in July, but is within the observed standard deviation for the other months. As at the Sde Boker and Bahrain sites, the α values are generally around 1 which indicates that the dust optical thickness is probably overestimated in the model.

These comparisons suggest that the model reproduces the optical thickness associated with major dust plumes over the oceans. The simulated background values in the northern hemisphere at 650 nm is 0.05-0.1. Near the dust sources, the simulated values are within the standard deviation of the AERONET data, with the exception of the Asian site. From these comparisons, it does not seem that the model overestimates

dust emissions.

3.6. Size distribution

Aerosol volume size distribution has been retrieved from the AERONET data by an iterative inversion algorithm [*Dubovik and King,* 2000]. The inversion algorithm calculates the effective size distribution for the total atmospheric column, assuming aerosol particles as polydisperse homogeneous spheres. *Dubovik et al.* [2000] showed that the size distribution can be retrieved reasonably well. For dust particles radius less than 0.3μm, retrieval problem associated with non-sphericity is avoided when the angular range of sky radiances is limited to scattering angles smaller than 30-40^0 (around noon). For larger dust particles, the limitation to small scattering angles does not apply. The size distribution has been retrieved at only a few sites (http://aeronet.gsfc.nasa.gov). Figure 11 shows the seasonal variation of the vertically integrated volume size distribution at Cape Verde, Banizoumbou, and Dalanzadgad, where the AERONET retrieved size distributions have been averaged over three months. The observed distribution generally shows a bimodal distribution with a fine (sulfate or carbonaceous aerosols) and a coarse mode with particles larger than 0.6μm. Only the coarse mode is of interest for this analysis.

At Cape Verde, the model reproduces the volume size distribution for each season, although it systematically underestimates the larger size fraction. The contribution of the largest fraction to the total mass is 5 times lower than the fraction centered at 1.5 μm. It thus seems that the lower than observed simulated optical thickness in June 1997 at Cape Verde is due to sub-scale perturbations unresolved by the model. At Banizoumbou, the model reproduces the maximum volume distribution at 1.5μm radius but overestimates the fraction below 1.5 μm and underestimates the fraction above. Also the model underestimates by 50% the size distribution at 1.5 μm in winter and spring. This could explain the lower than observed optical thickness in 1997 at

Banizoumbou (Figure 10).

At Dalanzadgad (Mongolia), the observed size distribution is quite different from that at Cape Verde and Banizoumbou. The coarse fraction is characterized by two modes: one with a mean radius at 1.5μm and the second with a mean radius at 7μm (Figure 11). The contribution of the second mode to the volume size distribution is dominant. This mode is outside the simulated particle size range. The model overestimates the first mode by a factor of 3 in spring and by a factor of 5 in summer. The overestimation of small dust particles compensates for the absence of particles larger than 6μm such that the simulated atmospheric dust load is comparable to the observations. This explains why the optical thickness (figure 10) and surface concentration (figure 4) near the Asian sources are not largely overestimated. However, because the lifetime of 1.5μm size particles is much longer than that of particles larger than 6μm, the overprediction of small particle emission will produce a model bias which is stronger far away from the source than near the source. Furthermore, we have seen (Plate 1) that dust plumes from Asian sources travel at high altitudes where the winds are stronger. We suspect that this efficient long range transport, especially for small particles, is at the origin of the too high background values of optical thickness (0.05-0.1) and surface concentration (5 times the observed value) estimated by the model over the North Pacific.

Finally, figure 11 highlights the large difference in the AERONET retrieved size distributions between the African and Asian stations which does not appear in the model results. In equation 2, the two variables which depend on the size distribution are the soil size fraction (s_p) and the threshold velocity (u_t). In our formulation, u_t is proportional to the square root of the particle radius. As we discussed in section 2.4, there is some evidence that below 30μm the threshold velocity is instead decreasing with the increase of radius. This could explain the lower than observed fraction of particles between 3 and 6 μm. The use of a more realistic parameterization (e.g. *Marticonera*

and Bergametti [1995]) might improve our results by increasing the fraction of large particles. But it will not help reproduce the large variability in size distribution between sites. This variability is most likely due to difference in soil properties. The value of s_p should be region specific, and in the case of Asia it should have a higher percentage of large particles. More measurements are needed to constrain the soil size distribution.

4. Conclusions

We have developed a new global dust source function which identifies the dust source locations at the topographically low regions with bare soil surface. This source function is a generalization of the finding in satellite data analysis [*Prospero et al.,* 2000] that the dust sources are associated with topographic depressions. The accumulation of sediments in these depressions during pluvial periods serves as a source of loose particles which can be easily uplifted into the atmosphere. We have generalized this finding and assume that all topographic lows have accumulated sediments which serve as potential dust sources.

With this distribution of dust sources, we have simulated the atmospheric dust distribution with the GOCART model which is driven by assimilated meteorological fields from the GEOS DAS. We have incorporated the emission, transport and removal processes of dust sizes ranging from 0.l to 6 μm radius. The model has been evaluated globally over a period of several years by comparing simulation results with observations of dust concentration at the surface, vertical distribution, surface deposition flux, optical thickness and size distribution.

We have been successful in reproducing observed global scale dust distribution patterns by considering dust emissions exclusively from these so-called 'hot-spots' regions. The total emission is estimated at 1604-1960 Tg yr^{-1}, in a 5-year simulation. This result is similar to other model results although distribution patterns differ substantially. The model source distribution allows to simulate the latitudinal shift of

dust plumes over the North Atlantic but does not always reproduce the low latitude of the aerosol plumes in winter. The contribution of aerosols from biomass burning is the most likely reason for the discrepancy in winter, rather than the contribution from disturbed sources that *Tegen and Fung* [1995] attributed to human activity. Also, other models which identify deserts as dust sources tend to greatly overestimate dust emissions in Australia. Our results did not show such a discrepancy because the model limits the source location to the Lake Eyre basin which is consistent with the analysis by *Prospero et al.,* [2000]. The comparison with LITE data shows that dust uplifting is simulated at the correct place and time, although the model does not reproduce all observed features in the vertical aerosol distributions.

Comparisons with observations have shown that the model is generally able to reproduce the seasonal variation of the surface concentration and optical thickness in the "dusty" regions (concentrations $> 2\mu$m). In remote regions where concentrations < 2 μm the model tends to overestimate the concentrations. Comparison with surface data is difficult because there is a large local variability which is not resolved by the model. Nevertheless, the model overestimates the surface concentration in the North Pacific by a factor of 3 to 5 which is much larger than the local variability. To understand the origin of this discrepancy, the dust concentration, vertical distribution, optical thickness, and size distribution have been compared with the observations in the vicinity of the Asian dust sources. The comparison did not show any significant discrepancy except for the size distribution. The model overestimates by a factor of 3 to 5 the size distribution at 1.5 μm while, in contrast, the observations show a peak at 7μm. Near the source, the overestimation of small particles compensates the absence of particle larger than 6μm radius and produces a simulated atmospheric dust load which is comparable to the observations. Far away from the sources, the atmospheric dust load is largely overestimated because small particles have a longer lifetime. Also our comparison with LITE data shows that Asian dust particles are uplifted efficiently

to 7-8 km altitude where they are subject to long range transport by the jet streams. Therefore, the atmospheric dust loading over the North Pacific is sensitive to the parameterization of dust uplifting and to the soil size distribution in Asian desert. From the comparison of the size distribution near the dust sources, it clearly appears that the size distribution differs significantly between the African and Asian soils. Past studies have been concentrated on dust characterization and mobilization over the Sahara, and there is little data available on Asian dust sources. This study shows that such data are needed to simulate correctly dust distribution over East Asia and the North Pacific.

Acknowledgments. We are very grateful to Andrea Molod for her continuous help with the DAO data and Richard Rood for providing the computational resources. We would like to thank Dennis Savoie, University of Miami, to provide us the measured dust concentrations at the surface. We are grateful to Didier Tanré for giving us access to the sunphotometers data at Cape Verde and Banizoumbou, and to Charles McClain for the sunphotometer data at Bahrain. Finally, we would like to thank the three anonymous reviewers for their fruitful comments. This work has been supported by the NASA Global Aerosol Climatology Program.

References

Allen, D. J., P. Kasibhatla, A. M. Thompson, R. B. Rood, B. G. Doddridge, K. E. Pickering, R. D. Hudson, and S.-J. Lin, Transport-induced interannual variability of carbon monoxide determined using a chemistry and transport model, *J. Geophys. Res., 101,* 28,655-28,669, 1996.

Arimoto, R., R. A. Duce, B. J. Ray, A. D. Hewitt, and J. Williams, Trace elements in the atmosphere of American Samoa: Concentrations and deposition to the tropical South Pacific, *J. Geophys. Res., 92,* 8465-8479, 1987.

Arimoto, R., B. J. Ray, R. A. Duce, A. D. Hewitt, R. Boldi, and A. Hudson, Concentrations, sources, and fluxes of trace elements in the remote marine atmosphere of New Zealand, *J. Geophys. Res., 95,* 22,389-22,405, 1990.

Avila, A., I. Queralt-Mithjans, and M. Alarcón, Mineralogical composition of African dust delvered by red rains over northeastern Spain, *J. Geophys. res., 101,* 21,977-21,996, 1997.

Belly, P. Y., Sand movement by wind, *US Army Coastal Eng. Res. Tech. Mem. I,* 38 pp., 1964.

Chiapello, I., G. Bergametti, B. Chatenet, P. Bousquet, F. Dulac, and E. Santos Soares, Origins of African dust transported over the northeastern tropical Atlantic, *J. Geophys. Res., 102,* 13701-13709, 1997.

Chin, M., R. B. Rood, S.-J. Lin, J.-F. Müller, and A. Thompson, Atmospheric sulfur cycle simulated in the global model GOCART: Model description and global properties, *J. Geophys. Res., 105,* 24,671-24,687, 2000.

Chin, M., P. Ginoux, S. Kinne, O. Torres, B. Holben, B. Duncan, R. Martin, J. Logan, A. Higurashi, and T. Nakajima, Tropospheric aerosol optical thickness from the GOCART model and comparisons with satellite and sunphotometer measurements, *submitted to J. Atmos. Sci.,* 2001.

Davidson C. I., J.-L. Jaffrezo, B. W. Mosher, J. E. Dibb, R. D. Borys, B. A. Bodhaine, R. A. Rasmussen, C. F. Boutron, U. Gorlach, H. Cachier, J. Ducret, J.-L. Colin, N. Z.

Heidam, K. Kemp, and R. Hillamos, Chemical constituents in the air and snow at Dye 3, Greenland- I. Seasonal variations, *Atmos. Environ., 27A,* 2709-2722, 1993.

De Angelis, M., and A. Gaudichet, Sharan dust deposition over Mont Blanc (French Alps) during the last 30 years, *Tellus, 43B,* 61-75, 1991.

Dentener, F. J., G. R. Carmichael, Y. Zhang, J. Lelieveld, and P. J. Crutzen, Role of mineral aerosol as a reactive surface in the global troposphere, *J. Geophys. Res, 101,* 22,869-22889, 1996.

DeFries, R. S. and J. R. G. Townshend, NDVI-derived land cover classification at a global scale, *Int. J. Remote Sensing, 15,* 3567-3586, 1994.

Dickerson, R. R., S. Kondragunta, G. Stenchikov, K. L. Civerolo, B. G. Doddrige, and B. N. Holben, The impact of aerosols on solar ultraviolet radiation and photochemical smog, *Science, 278,* 827-830, 1997.

Dubovik, O., and M. D. King, A flexible inversion algorithm for retrieval of aerosol optical properties from Sun and sky radiance measurements, *J. Geophys. Res., 105,* 20,673-20,696, 2000.

Dubovik, O., B. N. Holben, M. D. King, Y. J. Kaufman, A. Smirnov, T. F. Eck, and I. Slutsker, Accuracy assessments of aerosol optical properties retrieved from AERONET Sun and sky-radiance measurements, *J. Geophys. Res., 105,* 9791-9806, 2000.

Duce, R. A., P. S. Liss, J. T. Merrill, E. L. Atlas, P. Buat-Menard, B. B. Hicks, J. M. Miller, J. M. Prospero, R. Arimoto, T. M. Church, W. Ellis, J. N. Galloway, L. Hansen, T. D. Jickells, A. H. Knap, K. H. Reinhardt, B. Schneider, A. Soudine, J. J. Tokos, S. Tsunogai, R. Wollast, and M. Ahou, The atmospheric input of trace species to the world ocean, *Global Biogeochem. Cycles, 5,* 193-259,, 1991.

Duce, R. A., Sources, distributions, and fluxes of mineral aerosols and their relationship to climate, in *Dalhem Workshop on Aerosol Forcing of Climate,* edited by R. J. Charlson and J. Heintzenberg, pp. 43-72, John Wiley, Chichester, U.K., 1995.

Eck, T. F., B. N. Holben, J. S. Reid, O. Dubovik, A. Smironov, N. T. O'Neill, I. Slutsker, and S. Kinne, Wavelength dependence of the optical depth of biomass burning, urban, and desert dust aerosol, *J. Geophys. Res., 104,* 31,333-31,350, 1999.

Fuchs, N. A., *The Mechanics of Aerosols,* Pergamon Press, Oxford, 1964.

Franzén, L. G., M. Hjelmroos, P. Kallberg, E. Brorström-Lundén, S. Juntto and A.-L. Savolainen, The yellow snow episode of northern Fennoscandia, March 1991- A case study of long-distance transport of soil, pollen and stable organic compounds, *Atm. Envir., 28,* 3587-3604, 1994.

Galloway, J. N., D. L. Savoie, W. C. Keene and J. M. Prospero, The temporal and spatial variability of scavenging ratios for nss sulfate, nitrate, methanesulfonate and sodium in the atmosphere over the North Atlantic ocean, *Atmos. Env., 27A,* 235-250, 1993.

Ganor, E., and Y. Mamane, Transport of Saharan dust across the eastern Mediterranean, *Atmos. Environ., 16,* 581-587, 1982.

Genthon, C., Simulations of the long range transport of desert dust and sea-salt in a general circulation model, in *Precipitation, Scavenging and Atmospheric Surface Exchange,* edited by S. E. Schwartz and W. G. N. Slinn, Hemisphere Publ. Washington, 1992a.

Genthon, C., Simulations of desert dust and sea-salt aerosols in Antarctica with a general circulation model of the atmosphere, *Tellus, 44B,* 371-389, 1992b.

Gillette, D. A., and R. Passi, Modeling dust emission caused by wind erosion, *J. Geophys. Res., 93,* 14,233-14,242, 1988.

Guelle, W., Y. Balkanski, M. Schulz, B. Marticonera, G. Bergametti, C. Moulin, R. Arimoto, Kind . D. Perry, Modeling the atmospheric distribution of mineral aerosol: Comparison with ground measurements and satellite observations for yearly and synoptic time scales over the North Atlantic, *J. Geophys. Res., 105* 1997-2012, 2000.

Helfland, H. M., and J. C. Labraga, Design of a nonsingular level 2.5 second order closure model for prediction of atmospheric turbulence, *J. Atmos. Sci., 45,* 113-132, 1988.

Herman, J. R., P. K. Bhartia, O. Torres, C. Hsu, C. Seftor, and E. Celarier, Global distribution of UV-absorbing aerosols from Nimbus 7/TOMS data, *J. Geophys. Res., 102,* 16,911-16,922, 1997.

Hillel, D., *Introduction to soil physics*, Academic Press, San Diego, Calif., 1982.

Holben, B. N., T. F. Eck, and R. S. Fraser, Temporal and spatial variability of aerosol optical depth in the Sahel region in relation to vegetation remote sensing, *Int. J. Remote*

Sens., 12, 1147-1163, 1991.

Holben, B. N. T. F. Eck, I. Slutsker, D. Tanre, J. P. Buis, A. Setzer, E. Vermote, J. A. Reagan, Y. J. Kaufman, T. Nakajima, F. Lavenu, I. Jankowiak, and A. Smirnov, AERONET- A federated instrument network and data archive for aerosol characterization, *Rem. Sens. Env., 66(1),* 1-16, 1998.

Husar, R. B., J. M. Prospero, and L. L. Stowe, Characterization of tropospheric aerosols over the oceans with the NOAA advanced very high resolution radiometer optical thickness operational product, *J. Geophys. Res., 95,* 16,889-16,909, 1997.

Iversen, J. D., and B. R. White, Saltation threshold on Earth, Mars and Venus, *Sedimentology, 29,* 111-119, 1982.

Joussaume, S., Three dimensional simulations of the atmospheric cycle of desert dust particles using a general circulation model, *J. Geophys. Res., 95,* 1909-1941, 1990.

Karyampudi, M. V., S. P. Palm, J. A. Reagen, H. Fang, W. B. Grant, R. M. Hoff, C. Moulin, H. F. Pierce, O. Torres, E. V. Browell, and S. H. Melfi, Validation of the Saharan dust plume conceptual model using lidar, Meteosat, and ECMWF data, *Bull. Amer. Meteor. Soc., 80,* 1045-1076, 1999.

Levin, Z., E. Ganor, and V. Gladstein, The effects of desert particles coated with sulfate on rain formation in the eastern Mediterranean, *J. Applied Meteorology, 35,* 1511-1523, 1996.

Lin, S.-J., and R. B. Rood, Multidimensional flux-form semi-Lagrangian transport schemes, *Mon. Weather Rev., 124,* 2046-2070, 1996.

Mahowald, N., K. Kohfeld, M. Hansson, Y. Balkanski, S. P. Harrison, I. C. Prentice, M. Schulz, and H. Rodhe, Dust sources and deposition during the last glacial maximum and current climate: A comparison of model results with paleodata from ice cores and marine sediments, *J. Geophys. Res., 104,* 15,895-15,916, 1999.

Marticonera, B., and G. Bergametti, Modeling the atmospheric dust cycle: 1. Design of a soil-derived dust emission scheme, *J. Geophys. Res., 100,* 16,415-16,430, 1995.

Merrill, J. T., M. Uematsu, and R. Bleck, Meteorological analysis of long range transport of mineral aerosols over the North Pacific, *J. Geophys. Res., 94,* 8584-8598, 1989.

Prospero, J. M., R. T. Nees, and M. Uematsu, Deposition rate of particulate and dissolved aluminium derived from Saharan dust in precipitation at Miami, Florida, *J. Geophys. Res., 92,* 14,723-14,731, 1987.

Prospero, J. M. , M. Uenatsu, and D. L. Savoie, Mineral Aerosol Transport to the Pacific Ocean, in *Chemical Oceanography,* Academic Press, New York, 1989.

Prospero, J. M., The atmospheric transport of particles to the ocean, in *Particle Flux in the Ocean,* edited by V. Ittekkot, P. Schäffer, S. Honjo and P. J. Depetris, John Wiley & Sons, New York, 1996.

Prospero, J. M., P. Ginoux, O. Torres, and S. Nicholson, Environmental Characterization of Global Sources of Atmospheric Soil Dust Derived from the NIMBUS-7 TOMS Absorbing Aerosol Product, *submitted to J. Geophys. Rev.,* 2000.

Pye K., *Aeolian dust and dust deposits,* 2^d edition, Academic Press, San Diego, USA, 1989.

Rao, C. R. N., L. L. Stowe, E. P. McClain, and J. Sapper, Development and application of aerols remote sensing with AVHRR data from the NOAA satellites, in *Aerosol and Climate,* edited by P. V. Hobbs and M. P. McCormick, pp. 69-79, A. Deepak, Hampton, Virginia, 1988.

Scheffer, F., and P. Schachtschabel, *Lehrbuch der Bodenkunde,* 13^{th} edition, F. Enke, Frankfurt, Germany, 1992.

Schubert, S. D., R. B. Rood, and J. Pfaendtner, An assimilated data set for Earth science applications, *Bull. Am. Meteorol. Soc., 74,* 2331-2342, 1993.

Schulz, M., Y. J. Balkanski, W. Guelle, and F. Dulac, Role of aerosol size distribution and source location in a three-dimensional simulation of a Saharan dust episode tested against satellite-derived optical thickness, *J. Geophys. Res., 103,* 10,579-10,592, 1998.

Shao, Y., R. Raupach, and J. F. Leys, A model for predicting aeolian sand drift and dust entrainment on scales from paddock to region, *Aust. J. Soil. res., 34,* 309-342, 1996.

Smirnov, A., B. N. Holben, T. F. Eck, O. Dubovik, and I. Slutsker, Cloud-screening and qualtity control algorithms for the AERONET database, *Remote Sens. Environ., 73,* 337-349, 2000a.

Smirnov, A., B. N. Holben, D. Savoie, J. M. Prospero, Y. J. Kaufman, D. Tanre, T. F. Eck,

and I. Slutsker, Relationship between column aerosol optical thickness and in situ ground based dust concentrations over Barbados, *Geophys. Res. Lett., 27,* 1643-1646, 2000b.

Takacs, L. L., A. Molod, and T. Wang, Documentation of the Goddard Earth Observing System (GEOS) General Circulation Model-Version 1, Technical report series on global Modeling and Data Assimilation, *NASA Tech. Mem. 104606, vol.1*, Goddard Space Flight Center, Greenbelt, 100 pp., 1994.

Takamura, T., H. Okamoto, Y. Maruyama, A. Numaguti, A. Higurashi, and T. Nakajima, Global three-dimensional simulation of aerosol optical thickness distribution of various origins, *J. Geophys. Res., 105,* 17,853-17,873, 2000.

Tegen, I., and I. Fung, Modeling of mineral dust in the atmosphere: Sources, transport, and optical thickness, *J. Geophys. Res., 99,* 22,897-22,914, 1994.

Tegen, I., and I. Fung, Contribution to the atmospheric mineral aerosol load from land surface modification, *J. Geophys. Res., 100,* 18,707-18,726, 1995.

Tegen, I., and A. A. Lacis, Modeling of particle size distribution and its influence on the radiative properties of mineral dust aerosol, *J. Geophys. Res., 101,* 19,237-19,244, 1996.

Tegen, I., A. Lacis, and I. Fung, The influence of mineral aerosol from disturbed soils on the global radiation budget, *Nature, 380,* 419-422, 1996.

Tegen, I., P. Hollrig, M. Chin, I. Fung, D. Jacob, and J. Penner, Contribution of different aerosol species to the global aerosol extinction optical thickness: Estimates from model results, *J. Geophys. Res., 102,* 23,895-23,915, 1997.

Torres, O., P. K. Bhartia, J. R. Herman, Z. Ahmad, and J. Gleason, Derivation of aerosol properties from satellite measurements of backscattered ultraviolet radiation: Theoretical basis, *J. Geophys. Res., 103,* 17,099-17,110, 1998.

Velde, B., *Introduction to clay minerals*, Chapman and Hall, London, England, 1992.

Winker, D. M., R. H. Couch, and M. P. McCormick, An overview of LITE: NASA's Lidar In-space Technology Experiment, *Proc. IEEE, 84,* 164-180, 1996.

Zhang, X. Y., R. Arimoto, G. H. Zhu, T. Chen, and G. Y. Zhang, Concentration, size-distribution and deposition of mineral aerosol over Chinese desert regions, *Tellus, 50B,*

317-330, 1998.

P. Ginoux, NASA Godard Space Flight Center, Code 916, Greenbelt, MD 20771, USA. (e-mail: ginoux@rondo.gsfc.nasa.gov)

M. Chin, NASA Godard Space Flight Center, Code 916, Greenbelt, MD 20771, USA. (e-mail: chin@rondo.gsfc.nasa.gov)

I. Tegen, Max-Planck-Institute for Biogeochemistry, P.O. Box 10 01 64, 07701 Jena, Germany (e-mail: itegen@bgc-jena.mpg.de)

J. M. Prospero, Rosenstiel School of Marine and Atmospheric Science, University of Miami, 4600 Rickenbacker Causeway, Miami, FL 33149, USA. (e-mail: jprospero@rsmas.miami.edu)

B. Holben, NASA Godard Space Flight Center, Code 923, Greenbelt, MD 20771, USA. (e-mail: brent@aeronet.gsfc.nasa.gov)

O. Dubovik, NASA Godard Space Flight Center, Code 923, Greenbelt, MD 20771, USA. (e-mail: dubovik@aeronet.gsfc.nasa.gov)

S.-J. Lin, NASA Godard Space Flight Center, Code 910.3, Greenbelt, MD 20771, USA. (e-mail: slin@dao.gsfc.nasa.gov)

Received _____

To appear in the *Journal of Geophysical Research*, 2001.

Figure 1. Comparison between the dust source function (upper panel), and the dust emission (middle panel) and distributions of TOMS aerosol index (lower panel). The dust emission and TOMS aerosol index are average avlues from 1987 to 1990.

Figure 2. Seasonal variation of dust concentration, averaged over 5 years (1987-1990 and 1996), in units of μg m^{-3}.

Figure 3. Comparison of annual mean concentration simulated (bold line) and observed (dots) at 18 sites; the standard deviation of the simulated and observed values are represented by shading and vertical segments, respectively.

Figure 4. Comparison of monthlty dust concentration simulated and observed at 18 sites, in units of μg m^{-3}.

Figure 5. Zonal mean dust concentration with isolines at 0.5, 1, 5, 10 and 50 μg m^{-3}.

Figure 6. Global distribution of the annual total deposition flux [g m^{-2}.yr^{-1}], averaged over 5 years simulation (1987-1990 and 1996).

Figure 7. Comparison of annual total deposition flux simulated and observed at 16 sites.

Figure 8. Comparison of the mean optical thicknesses simulated at 650 nm (upper panel) and observed at 630 nm by AVHRR (lower panel), from 1987 to 1990.

Figure 9. Latitudinal variation of the maximum optical thickness along the 25^{o}W meridian deduced from AVHRR data (continuous line) between January 1987 and December 1990 (November 1988 is missing), and from the model simulations (dashed line).

Figure 10. Comparison of optical thicknesses simulated (bold line) and measured by AERONET (dots) at 6 sites; the standard deviation of the simulated and observed values are represented by shading and vertical segments, respectively. The lower panels give the monthly Angstrom parameter, α, calculated from the AERONET optical thicknesses at 440 and 670 nm.

Figure 11. Comparison of volume size distribution [μm^3.μm^{-2}] simulated (dashed line) and retrieved (continuous line) from AERONET data.

Plate 1. Vertical sections, from the surface to 10 km altitude, of aerosols the 17^{th} of September 1994 over the Sahara (orbit 115) and China (orbit 125). The top and third panels are the LITE raw signal at 532 nm. The second and bottom panels are the simulated dust concentration (μg m^{-3}) along the same orbits.

Table 1. GEOS DAS Meteorological fields used as model input

Variable	Time Resolution
- Prognostic -	
Surface pressure	6 hours, instantaneous
Temperature	6 hours, instantaneous
Wind velocity	6 hours, instantaneous
Specific humidity	6 hours, instantaneous
Surface wetness	6 hours instantaneous
- Diagnostic -	
Cloud mass flux	6 hours, averaged
Specific humidity changes due to moist processes	6 hours, averaged
Wind speed at 10 meters	3 hours, averaged
Precipitation	3 hours, averaged
Eddy diffusion	3 hours, averaged

Table 2. Annual budget of dust for the years 1987-1990 and 1996: emission (Em), dry deposition (Dry), wet deposition (Wet), atmospheric burden (Load), and lifetime (Life).

Year	Emis.	Dry	Wet	Load	Life
	Tg yr^{-1}	Tg yr^{-1}	Tg yr^{-1}	Tg	day
1987	1883	1653	256	38	7.1
1988	1956	1704	289	40	7.3
1989	1804	1613	229	36	7
1990	1829	1611	237	34	6.6
1996	1604	1451	166	31	6.6

There is a 2% difference between the total emission and total deposition due to numerical errors in the advective scheme.

Table 3. Annual budget, averaged over 5 years (1987-1990 and 1996) for each size classes: emission (Em), dry deposition (Dry), wet deposition (Wet), atmospheric burden (Load), and lifetime (Life).

Size μm	Emis. Tg yr^{-1}	Dry Tg yr^{-1}	Wet Tg yr^{-1}	Load Tg	Life day
0.1-1	335	265	79	14	14
1-2	571	484	97	14.5	9
2-3	504	461	49	6.1	4.3
3-6	404	396	10	1.3	1.1
0.1-6	1814	1606	235	35.9	7.1

Table 4. Total simulated deposition (Tg yr^{-1}) to various ocean regions compared with estimated values by *Duce et al.* [1991] and *Prospero* [1996].

Ocean	*Duce et al.*, 1991	*Prospero*, 1996	GOCART
North Pacific	480	96	92
South Pacific	39	8	28
North Atlantic	220	220	184
South Atlantic	24	5	20
North Indian	100	20	138
South Indian	44	9	16
Global	910	358	478

Table 5. List of stations managed by the Rosenstiel School of Marine and Atmospheric Science (University of Miami) for the measurement of atmospheric dust concentration.

	Name	Latitude	Longitude
1	Barbados	13.17^{o}N	59.43^{o}W
2	Miami	25.75^{o}N	80.25^{o}W
3	Bermuda	32.27^{o}N	64.87^{o}W
4	Izana	28.3^{o}N	16.5^{o}W
5	Mace Head	53.32^{o}N	9.85^{o}W
6	King George	62.18^{o}S	58.3^{o}W
7	Cape Point	34.35^{o}S	18.48^{o}E
8	Kaashidoo	4.95^{o}N	73.45^{o}E
9	Cheju	33.52^{o}N	126.48^{o}E
10	Hedo	26.92^{o}N	128.25^{o}E
11	Enewetak	11.33^{o}N	162.3^{o}E
12	Midway	28.22^{o}N	177.35^{o}W
13	Oahu	21.33^{o}N	157.7^{o}W
14	Nauru	0.53^{o}S	166.95^{o}E
15	Funafuti	8.5^{o}S	179.2^{o}W
16	New Caledonia	22.15^{o}S	167^{o}E

Table 5. (continued)

	Name	Latitude	Longitude
17	Cape Grim	40.68^{o}S	144.68^{o}E
18	Norfolk Isl.	29.08^{o}S	167.98^{o}E

Table 6. Model versus observed total dust deposition fluxes (g m^{-1} yr^{-1}) at 16 sites.

	Location	Latitude	Longitude	Meas Years	Meas[a]	GOCART[b]
1	Shemya	52.92^{o}N	174.06^{o}E	1981-1987	0.6	0.9 ± 0.1
2	French Alps	45.5^{o}N	6.5^{o}E	1955-1985	2.1	2.6 ± 0.5
3	Spain	41.8^{o}N	2.3^{o}E	1987-1990	5.3 ± 2.6	3.3 ± 0.6
4	Midway	28.2^{o}N	177.35^{o}W	1981-1987	0.6 (0.3-1.1)	1.8 ± 0.1
5	Miami	25.75^{o}N	80.25^{o}W	1982-1983	1.62	3.3 ± 0.5
6	Oahu	21.3^{o}N	157.6^{o}W	1981-1987	0.42 (0.4-0.5)	1.3 ± 0.2
7	Enewetak	11.3^{o}N	162.3^{o}E	1981-1987	0.44	0.9 ± 0.3
8	Fanning	3.9^{o}N	159.3^{o}W	1981-1987	0.09 (0.05-0.22)	0.4 ± 0.1
9	Nauru	0.53^{o}S	166.95^{o}E	1981-1987	0.23	0.35 ± 0.1
10	Samoa	14.25^{o}S	170.6^{o}W	1981	0.15 (0.02-0.22)	0.35 ± 0.07
11	Rarotonga	21.25^{o}S	159.75^{o}W	1981-1987	0.21	0.23 ± 0.04
12	New Caledonia	22.15^{o}S	167^{o}E	1983-1985	0.37	0.25 ± 0.05
13	Norfolk Isl.	29.08^{o}S	167.98^{o}E	1983-1987	0.64	0.3 ± 0.06
14	New-Zealand	34.5^{o}S	172.75^{o}E	1983	0.14 (0.1-1)	0.25 ± 0.05
15	Taklimakan	40^{o}N	85^{o}E	1994	450 (110-1900)	133 ± 7
16	Tel Aviv	32^{o}N	34.5^{o}E	1972	30 (20-40)	11 ± 0.7

a. References: *Prospero et al.* [1989] for sites 1, 4, 6, 7, 8, 9, 11, 12, and 13; *Angelis and Gaudichet* [1991] for site 2, *Avila et al.* [1997] for site 3; *Prospero et al.* [1987] for site 5; *Arimoto et al.* [1987] for site 10; *Arimoto et al.* [1990] for site 14; *Zhang et al.* [1998] for site 15; *Ganor and Mamane* [1982] for site 16.

b. model results are 5 years (1987-1990 and 1996) average.

Table 7. Site name, latitude, longitude, selected year of measurements and corresponding year of simulation for each AERONET sites used for comparison.

	Name	Latitude	Longitude	Year Obs	Year Model
1	Barbados	13.2N	59.5W	1997	1997
2	Cape Verde	16.7N	22.9W	1997	1997
3	Banizoumbou	13.5N	2.65E	1996	1996
4	Sde Boker	30.5N	34.5E	1996	1996
5	Bahrain	26.3N	50.5E	1998-1999	1996-1997
6	Dalanzadgad	43.6N	104.4E	1997	1997

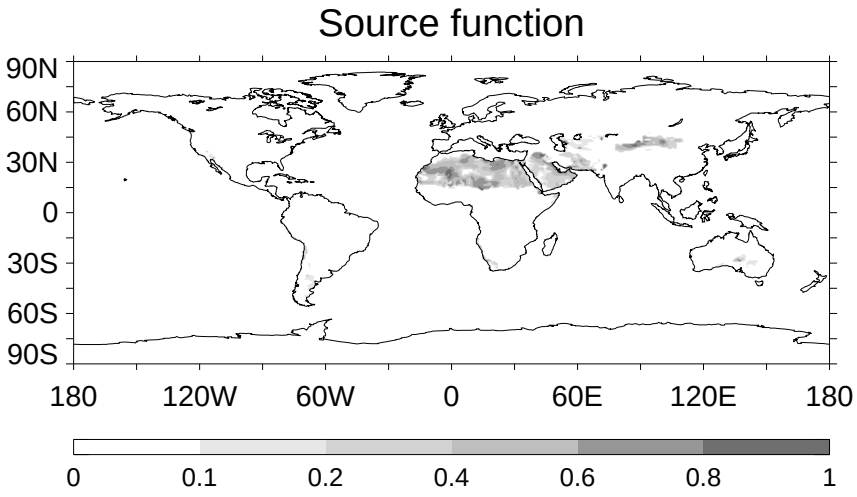
Source function
90N
60N
30N
0
30S
60S
90S
180
120W
60W
0
60E
120E
180
0
0.1
0.2
0.4
0.6
0.8
1

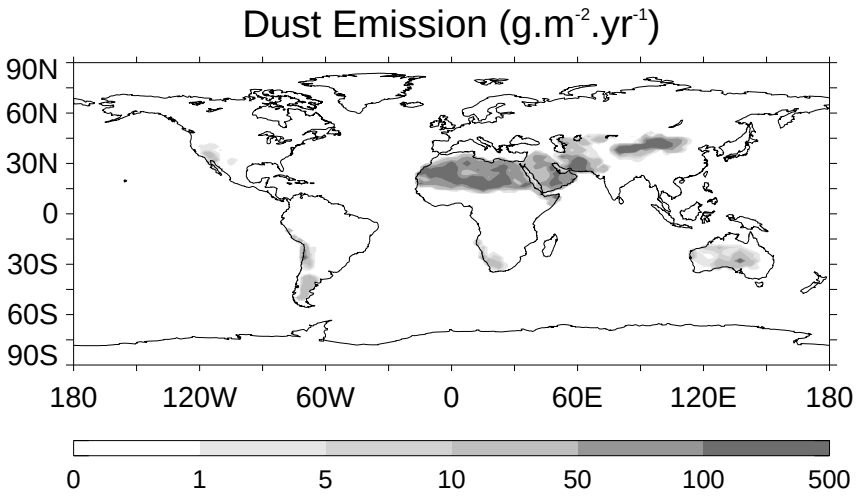
Dust Emission (g.m-2.yr-1)
90N
60N
30N
0
30S
60S
90S
180
120W
60W
0
60E
120E
180
0
1
5
10
50
100
500

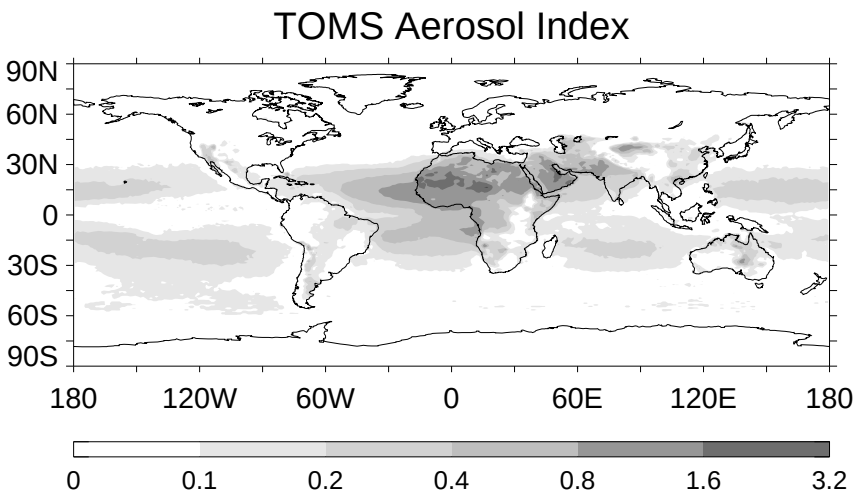
TOMS Aerosol Index
90N
60N
30N
0
30S
60S
90S
180
120W
60W
0
60E
120E
180
0
0.1
0.2
0.4
0.8
1.6
3.2

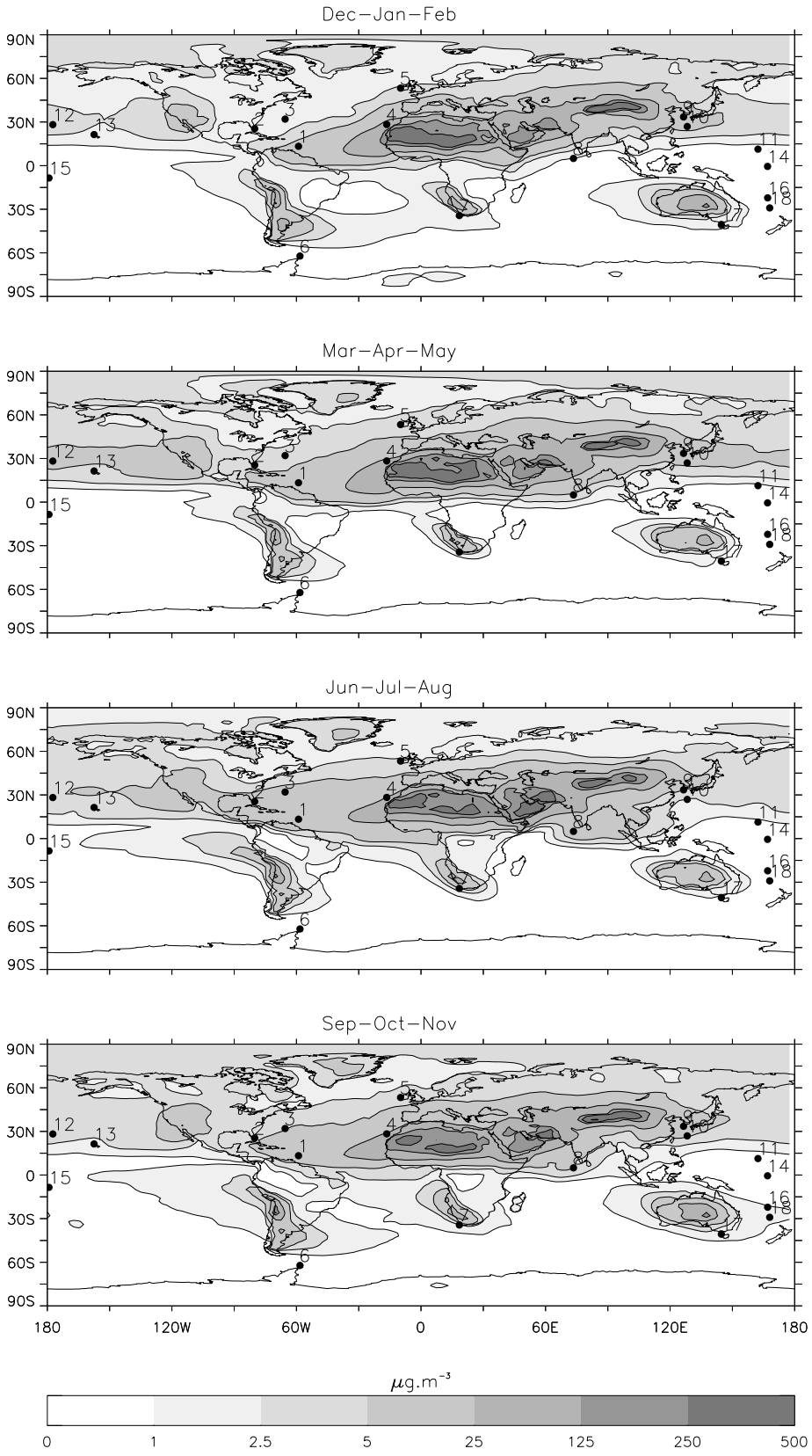
Dec–Jan–Feb
Mar–Apr–May
Jun–Jul–Aug
Sep–Oct–Nov
90N
60N
30N
0
30S
60S
90S
180
120W
60W
0
60E
120E
180
μg.m⁻³
0
1
2.5
5
25
125
250
500

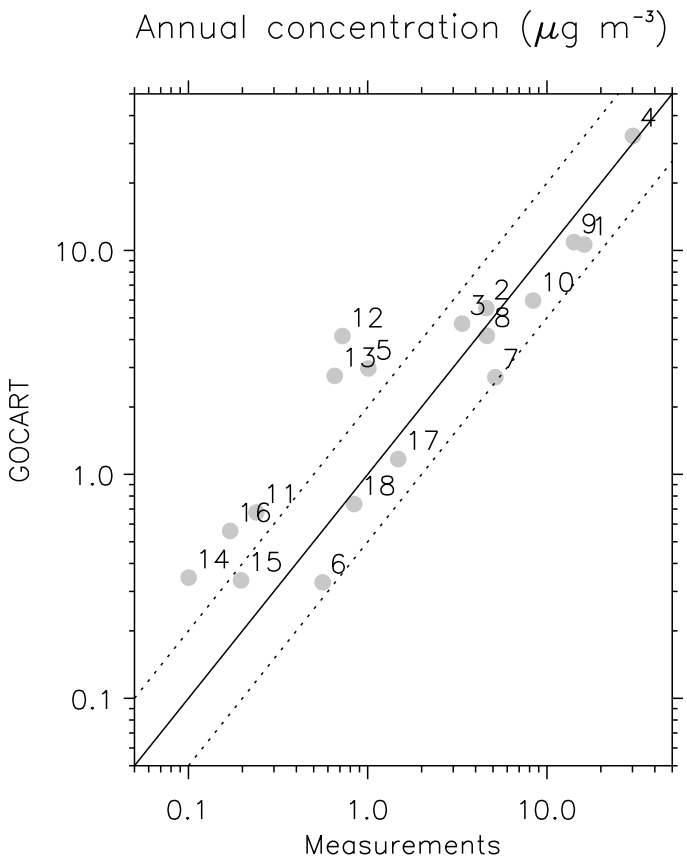
Annual concentration (μg m⁻³)
GOCART
Measurements
0.1
1.0
10.0
4
9
1
10
3
2
8
12
13
5
7
17
18
11
16
14
15
6

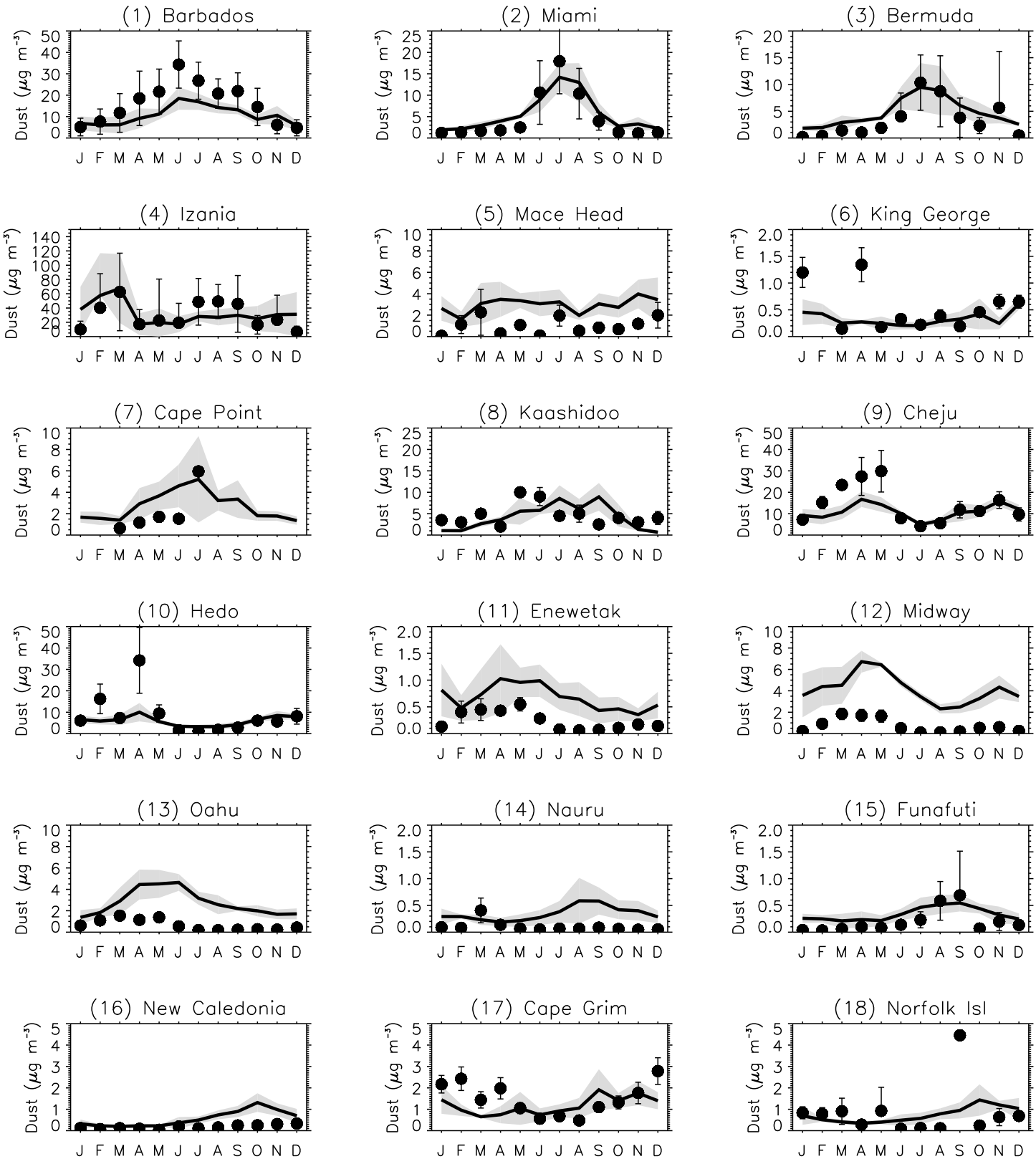
(1) Barbados
(2) Miami
(3) Bermuda
(4) Izania
(5) Mace Head
(6) King George
(7) Cape Point
(8) Kaashidoo
(9) Cheju
(10) Hedo
(11) Enewetak
(12) Midway
(13) Oahu
(14) Nauru
(15) Funafuti
(16) New Caledonia
(17) Cape Grim
(18) Norfolk Isl
Dust (μg m⁻³)
J F M A M J J A S O N D

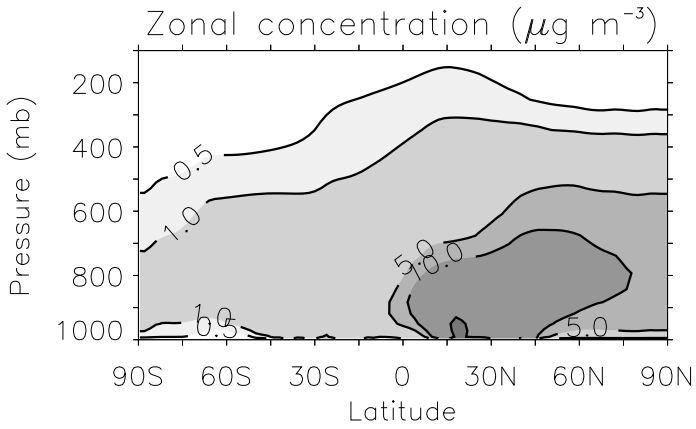
Zonal concentration (μg m^{-3})
Pressure (mb)
200
400
600
800
1000
0.5
1.0
5.0
10.0
1.0
0.5
5.0
90S
60S
30S
0
30N
60N
90N
Latitude

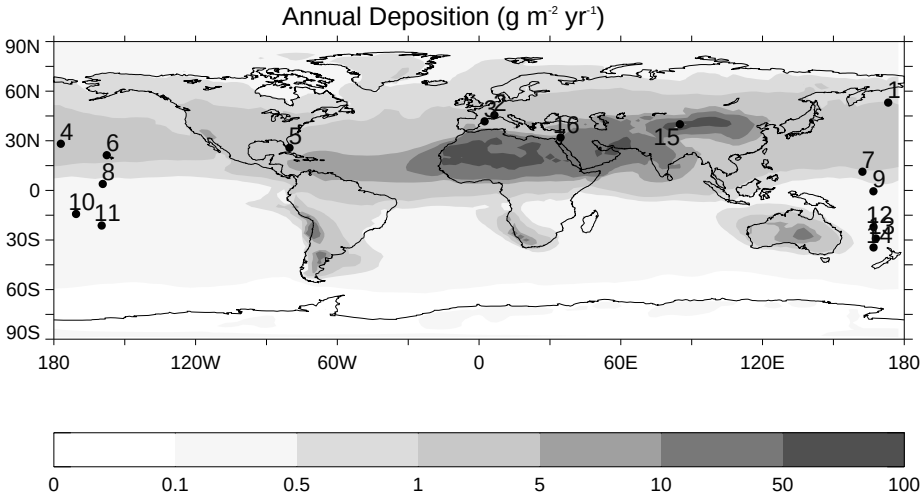
Annual Deposition (g m-2 yr-1)
90N
60N
30N
0
30S
60S
90S
180
120W
60W
0
60E
120E
180
1
4
5
6
7
8
9
10
11
12
15
0
0.1
0.5
1
5
10
50
100

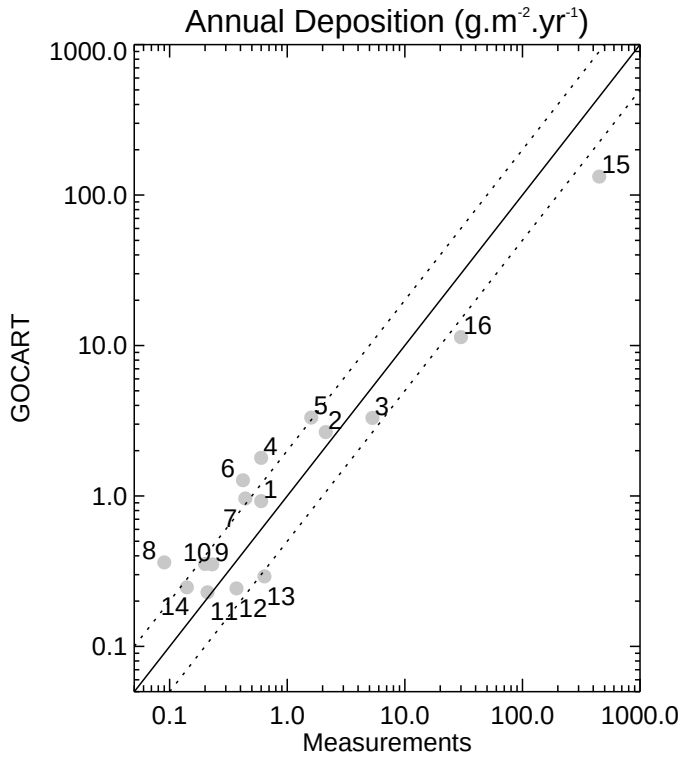
Annual Deposition (g.m-2.yr-1)
GOCART
Measurements
1000.0
100.0
10.0
1.0
0.1
0.1
1.0
10.0
100.0
1000.0
1
2
3
4
5
6
7
8
9
10
11
12
13
14
15
16

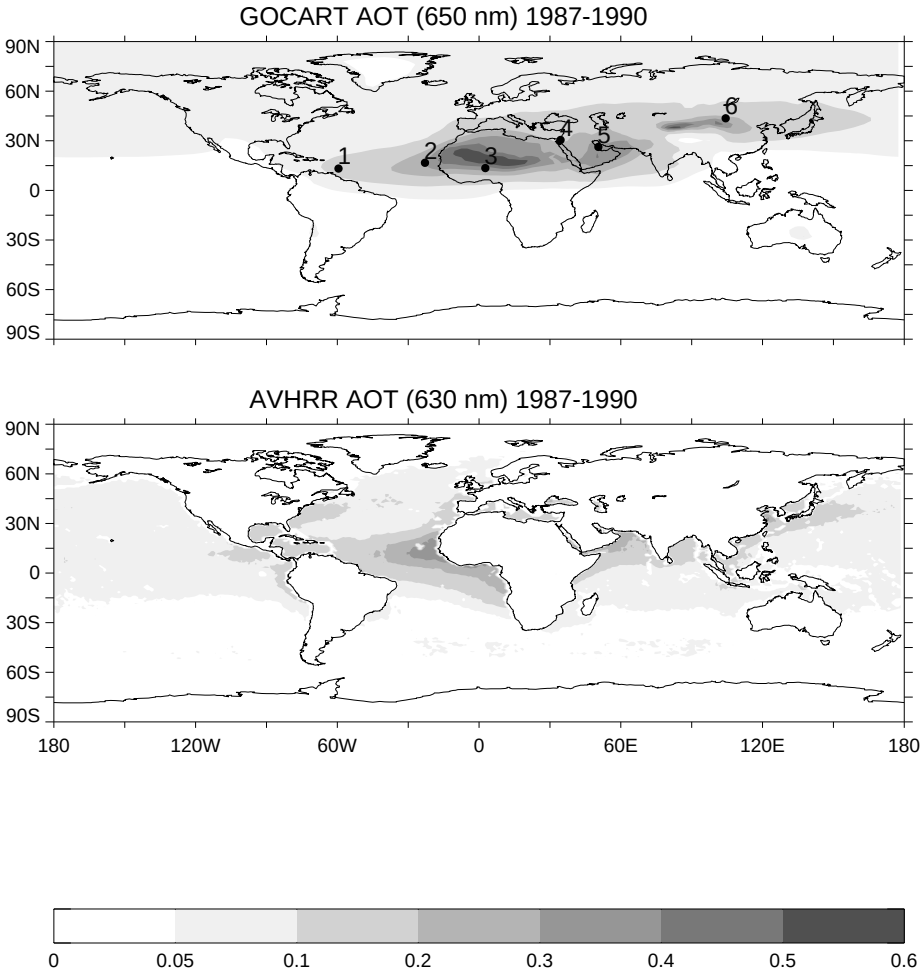
GOCART AOT (650 nm) 1987-1990
90N
60N
30N
0
30S
60S
90S
1
2
3
4
5
6
AVHRR AOT (630 nm) 1987-1990
90N
60N
30N
0
30S
60S
90S
180
120W
60W
0
60E
120E
180
0
0.05
0.1
0.2
0.3
0.4
0.5
0.6

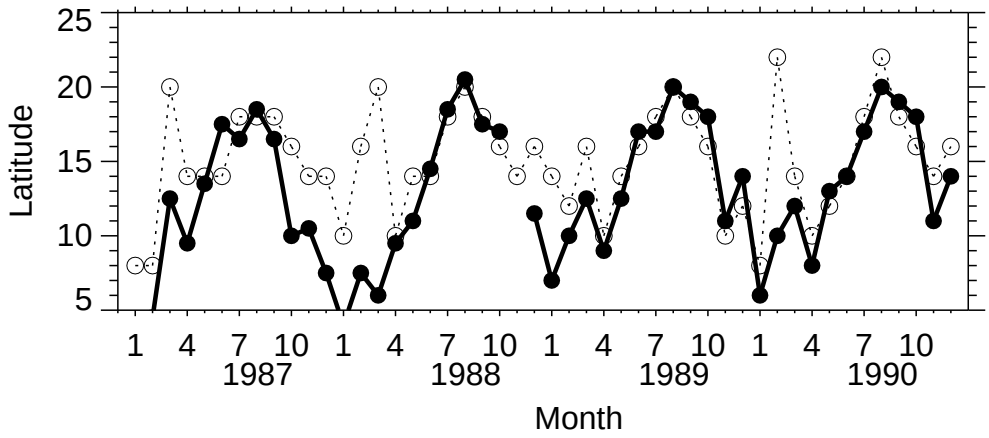
25
20
15
10
5
Latitude
1
4
7
10
1987
1988
1989
1990
Month

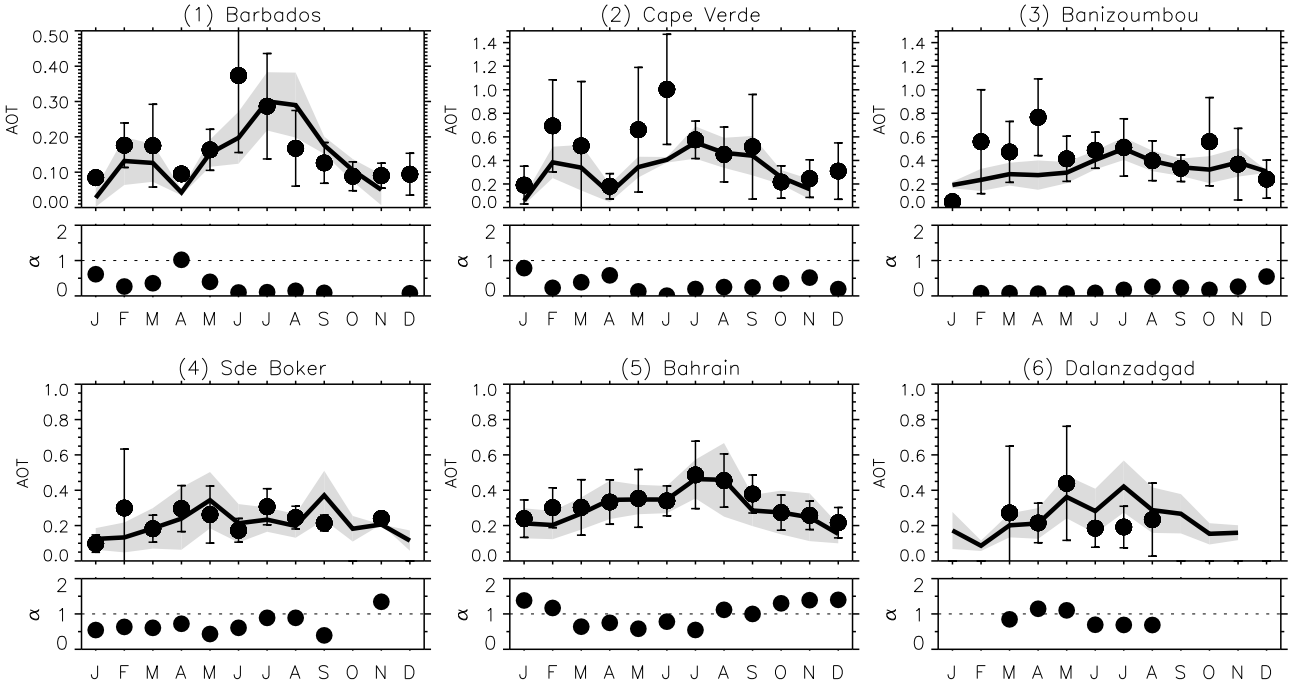
(1) Barbados
(2) Cape Verde
(3) Banizoumbou
(4) Sde Boker
(5) Bahrain
(6) Dalanzadgad
AOT
α
J F M A M J J A S O N D

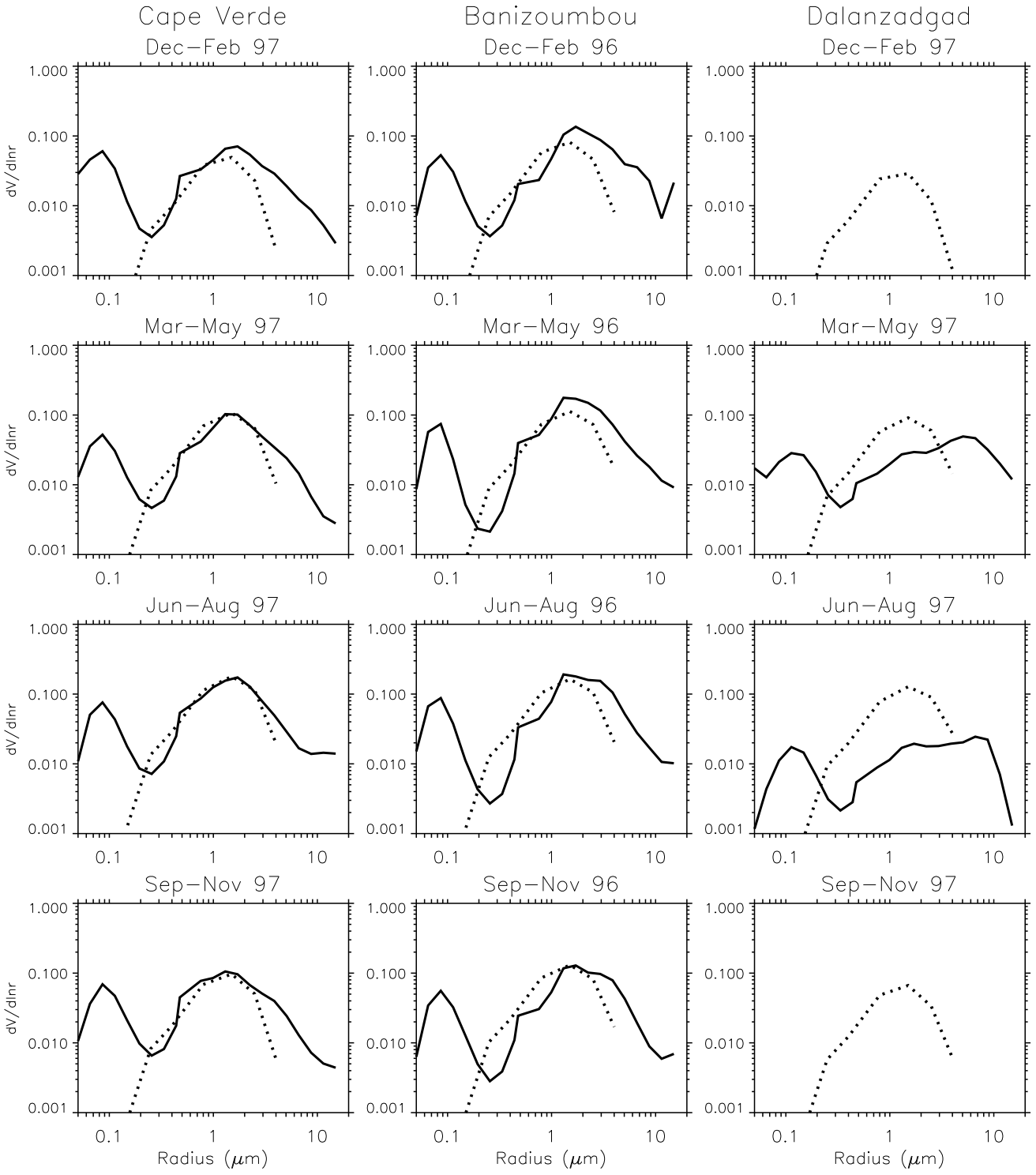
Cape Verde
Banizoumbou
Dalanzadgad
Dec–Feb 97
Dec–Feb 96
Dec–Feb 97
Mar–May 97
Mar–May 96
Mar–May 97
Jun–Aug 97
Jun–Aug 96
Jun–Aug 97
Sep–Nov 97
Sep–Nov 96
Sep–Nov 97
dV/dlnr
1.000
0.100
0.010
0.001
0.1
1
10
Radius (μm)

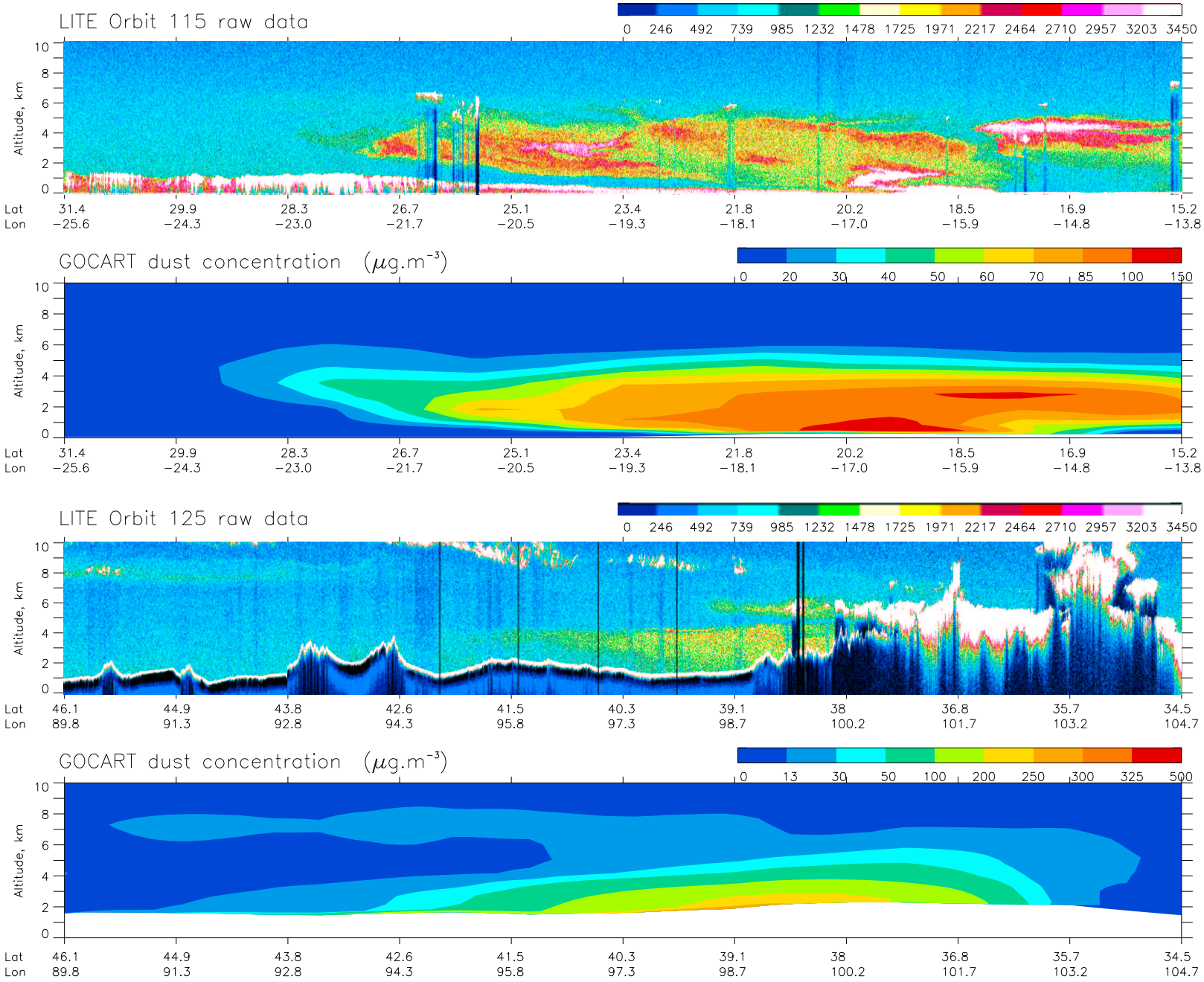

Plate 1. Comparison of LITE backscattering ratio at 532 nm with simulated dust concentration (ug/m3) along the orbits 115 and 125